Synthetic Point-on-Wave Dataset for Benchmarking Subsynchronous Oscillation Source Localization Techniques

Pablo Gill Estevez
University of Buenos Aires
Buenos Aires, Argentina
pgill@fi.uba.ar

Slava Maslennikov
ISO New England
Holyoke, USA
smaslennikov@iso-ne.com

Bin Wang
ISO New England
Holyoke, USA
bwang@iso-ne.com

***Abstract*—This work introduces a set of test cases designed to evaluate methods for locating sources of subsynchronous oscillations (SSO). The dataset consists of synthetic point-on-wave measurements generated through electromagnetic transient (EMT) simulations using SimplusGT, an open-source software tool developed at Imperial College London. The test cases cover a range of system conditions intended to replicate observed and potential SSO phenomena in power systems with high renewable penetration. This dataset serves as a benchmark for validating and comparing the performance of different SSO localization techniques.**

***Index Terms*—oscillation source location, subsynchronous oscillations, point-on-wave data, energy functions, dissipating energy flow, test cases.**

I. Introduction

The increasing integration of renewable energy sources and power electronic converters has introduced new dynamic behaviors in power systems, including subsynchronous oscillations (SSO) [1], [2]. These oscillations, which occur at frequencies below the system's fundamental frequency, can threaten system stability and even damage critical equipment. For example, the 2009 SSO event in Texas resulted in significant damage to many wind turbines.

Accurately identifying the sources of these oscillations is essential for developing effective mitigation strategies and ensuring the secure operation of the power grid. Oscillation source location (OSL) methods are typically categorized into model-based and measurement-based approaches [3]. Model-based methods commonly rely on techniques such as eigenvalue analysis [4] and impedance analysis [5] [6]. However, these approaches are less effective for forced oscillations (FO) and are often constrained by the lack of detailed (gray-box) models and high computational requirements. As a result, they are mainly suitable for offline risk assessment rather than real-time monitoring [7]. In contrast, measurement-based methods do not require a large-scale system model and involve significantly lower computational effort, making them more suitable for online applications. Examples include the sub/super-synchronous power (SSP) method, impedance-based methods, and energy-based approaches. Both the SSP and impedance methods identify negative resistance behavior associated with SSO, sharing a common underlying physical mechanism [7]. Energy-based methods, on the other hand, calculate the dissipating energy flow caused by the oscillation and trace it back to the component injecting energy into the system, which is identified as the source of the oscillation [8] [9] [10]. An up-to-date review of OSL methods can be found in [11].

Validating and benchmarking OSL techniques requires access to high-quality, realistic datasets generated under controlled conditions. Existing datasets primarily rely on PMU measurements [12], whose usefulness is largely limited to natural or forced oscillations within the electromechanical frequency range. However, for inverter-based resource (IBR)-induced high-frequency SSO, the oscillation magnitude and phase captured by PMU can be significantly distorted due to the inherent limitations of the underlying estimation algorithms. To address this gap, point-on-wave (PoW) datasets, offering direct, high-resolution voltage and current waveforms, are needed but currently unavailable.

This paper presents a comprehensive PoW dataset generated via electromagnetic transient (EMT) simulations using SimplusGT, an open-source simulation platform developed at Imperial College London [13]. The simulated scenarios cover a range of network configurations and excitation mechanisms known to induce SSO, including both natural and forced oscillations involving grid-following (GFL) and grid-forming (GFM) inverters. The resulting dataset is designed to facilitate the evaluation and benchmarking of both existing and emerging SSO source localization techniques. The dataset is publicly available through the dataset library [14] of the IEEE Task Force on Forced Oscillations [15]. Each case includes 60 seconds of three-phase bus voltage and injection current waveforms at all buses, sampled at 500 Hz.

II. Grid Following Inverters-Induced Natural Oscillations

Fig. 1 shows an extension of the IEEE 14-bus system, developed in [16], with grid-following (GFL) inverters added at buses 11, 12, and 13, denoted as A11, A12, and A13. The locations of A12 and A13 were selected at adjacent buses

979-8-3315-8138-1

within the weakest area of the system in terms of short-circuit level, while A11 was placed electrically slightly farther away but still within the same area. It is worth noting that stability issues of GFL inverters are more pronounced under conditions of relatively low short-circuit strength.

The IEEE 14-bus system model is available as one of the base cases in the SimplusGT library. This extended model is built upon a modified IEEE 14-bus system, incorporating the generator, excitation system, and turbine-governor parameters from [17]. Load models are represented as RL elements, and the system base is set to 100 MVA.

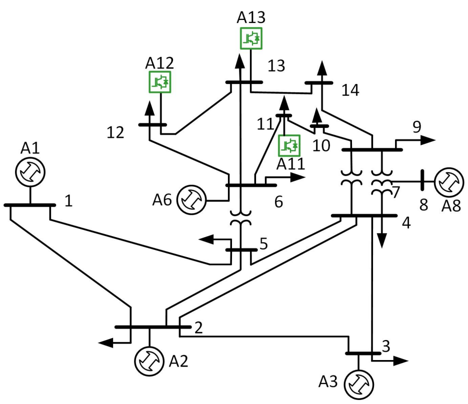

Fig. 1. Modified IEEE 14-bus system with added GFL inverters connected at buses 11, 12, 13 [16]

The control scheme of the GFL inverter is illustrated in Fig. 2. GFL inverters employs a synchronous-reference-frame control structure based on a phase-locked loop (PLL), which provides the grid voltage angle for the dq transformations. The measured three-phase currents are transformed into the dq frame and regulated by inner current control loops to track the reference currents i_d^* and i_q^*. The outputs of the current controllers are converted back to the abc frame and applied to the pulse-width modulation (PWM) stage to generate the inverter switching signals. For the natural-oscillation cases, a GFL model that includes the DC-link voltage control is employed, whose output provides the i_d^* reference, as represented by the block shown in Fig. 3.

The key parameters include the DC-link voltage V_{dc}, DC-link capacitance C_{dc}, series output reactance X, series resistance R, and the control bandwidths of the DC-link voltage regulator (f_{vdc}), the phase-locked loop (PLL) (f_{PLL}), and the current control loop (f_{i}). Based on these parameters, the proportional–integral (PI) controller gains are determined as shown in Fig. 3. It is worth noting that the bandwidth parameters define the controller gains and represent the actual closed-loop bandwidths only if adequate time-scale separation is achieved. Therefore, these parameters should be regarded as target bandwidths for each control loop.

Cascaded control architectures rely on a clear separation of time scales between inner and outer control loops to enable approximate decoupling and independent controller design. Inner loops are designed with significantly higher bandwidth to ensure fast tracking of actuator-related variables, while outer loops operate at lower bandwidths and generate references for the inner controllers. A common design guideline is to maintain at least one order of magnitude separation between the bandwidths of consecutive loops. If this condition is not satisfied, strong dynamic coupling arises, resulting in reduced stability margins and the possible emergence of poorly damped or unstable oscillatory modes.

In GFL inverters, this principle is particularly critical due to the presence of the PLL, which introduces an additional dynamic loop associated with grid synchronization. The PLL bandwidth is typically selected well below that of the current controller and above that of the outer power or DC-link voltage control loops. Excessively fast PLL dynamics may interact with the current controller and network impedance, especially in weak grids, leading to oscillatory behavior, whereas overly slow PLL dynamics degrade phase-tracking performance. If the PLL bandwidth is not sufficiently separated from that of the DC-link voltage controller, the DC-link controller operates based on a slowly varying reference frame, which may lead to strong dynamic coupling between the DC-voltage loop and the PLL, reduced phase margin, and the emergence of low-frequency oscillations or instability.

A total of four natural oscillation cases involving GFL inverters are analyzed, labeled Case 1 through Case 4. Cases 1 to 3 are adopted from [18], while Case 4 represents a slight variation of Case 3. The control bandwidth parameters for each GFL inverter are summarized in Table I. The remaining parameters are identical across the GFL inverters and are set to: $V_{\mathrm{dc}} = 2.5$ pu, $C_{\mathrm{dc}} = 1.25$ pu, $X = 0.025$ pu, and $R = 0.001$ pu.

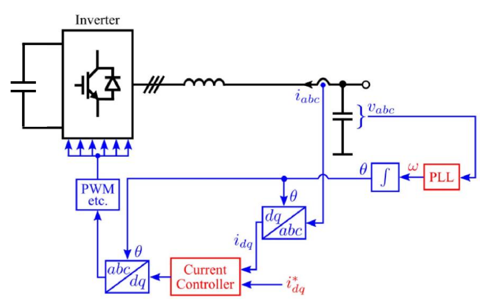

Fig. 2. Control diagram of the GFL inverter [19]

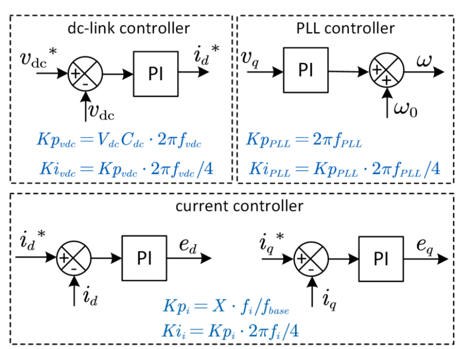

Fig. 3. PI Controllers diagram of the GFL inverter, e_{dq} is the inverter leg voltage, v_{dq} is the filter terminal voltage [20]

979-8-3315-8138-1

TABLE I
CONTROL BANDWIDTH OF GFL CASES 1 TO 4

Case	GFL	Bandwidth f_{vdc} (Hz)	Bandwidth f_{PLL} (Hz)	Bandwidth f_i (Hz)
1	A11	7	5	280
	A12	7	5	180
	A13	7	5	280
2	A11	7	10	1000
	A12	7	10	1000
	A13	7	10	1000
3	A11	10	20	450
	A12	10	30	320
	A13	10	20	450
4	A11	6	6	450
	A12	10	30	330
	A13	10	35	330

1) Case 1: GFL Current-PLL Oscillation (8.6 Hz): The current control bandwidths of inverters A11, A12, A13 were deliberately reduced to 280 Hz for A11 and A13, and 180 Hz for A12, with A12 exhibiting the weakest tuning. Fig. 4 shows the temporal evolution of the active power, reactive power, voltage magnitude, and voltage angle of inverters A11, A12, and A13. It can be observed that the oscillation exhibits harmonics.

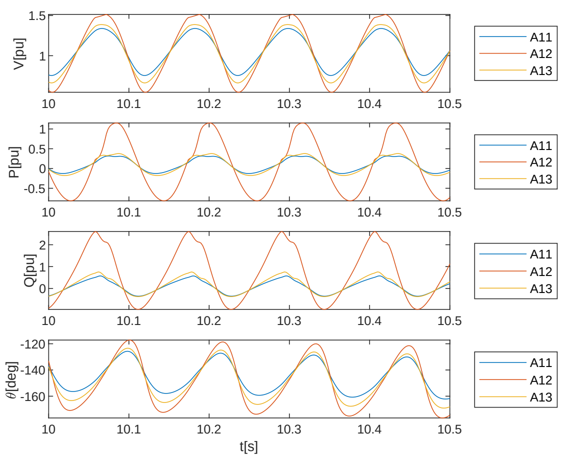

Fig. 4. Case 1. Time-domain responses of selected variables.

Fig. 5 shows an 8.6 Hz oscillation in the dq reference frame in the spectrogram of the active power of A12, accompanied by lower-amplitude harmonics at 17.2 and 25.8 Hz. These components correspond to sub- and super-synchronous oscillations in the abc frame, as evidenced in the spectrogram of the line current of A12 shown on the right-hand side of Fig. 5. In this particular case, the 58.6 Hz super-synchronous component is dominant over the 41.4 Hz sub-synchronous component. However, which component exhibits a higher magnitude depends on the network characteristics and the connected devices at each frequency, and therefore it cannot be generalized that one component will always be larger than the other.

2) Case 2: Control Interaction between GFL Inverters and Synchronous Generators (1.47 Hz): The output power of inverters A11, A12 and A13 was increased from 0.1 pu to 1.3

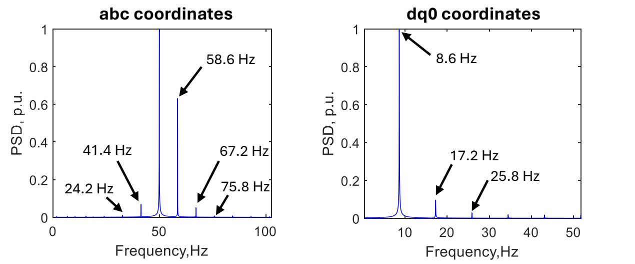

Fig. 5. Power spectral density in Case 1. Line current of A12 in the abc frame and active power of A12 in the $dq0$ frame.

pu (system base) while the output power of the synchronous generator A1 was reduced accordingly to balance the system. Because the governor of generator A1 constrains the mechanical power to non-negative values, the system operates with sustained oscillations at an off-nominal frequency of 51.7 Hz, as shown in Fig. 6. This deviation from the nominal 50 Hz does not affect the underlying control interactions between the synchronous generators and the IBRs.

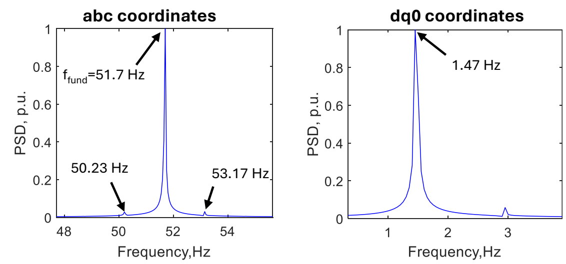

Fig. 6. Power spectral density in Case 2. Line current of A12 in the abc frame and active power of A12 in the $dq0$ frame.

3) Case: 3 GFL Current-PLL Oscillation (22.15 Hz): Modifications to the PLL, current-control, and DC control bandwidths of all IBRs resulted in a sustained oscillation at 22.15 Hz in the dq reference frame, with corresponding sideband components observed at 27.85 Hz and 72.15 Hz in the abc frame (Fig. 7). To shift the oscillatory mode frequency, the PLL control bandwidths were increased to 20 Hz for A11 and A13, and to 30 Hz for A12. In parallel, the current-control bandwidths were reduced to 450 Hz for A11 and A13, and 320 Hz for A12. The parameter tuning process was assisted by the Modal Analysis App embedded in SimplusGT, which provides modal frequency and damping sensitivity reports for each parameter and calculates the damping contributions of generators and inverters [6].

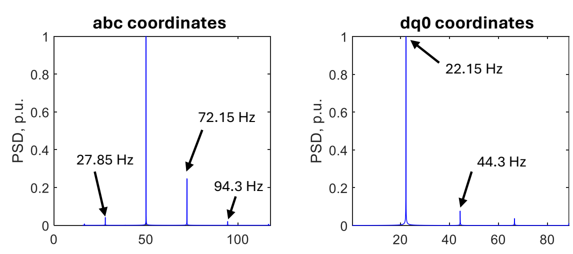

Fig. 7. Power spectral density in Case 3. Line current of A12 in the abc frame and active power of A12 in the $dq0$ frame.

979-8-3315-8138-1

4) Case 4: GFL Current-PLL Oscillation (19 Hz): In this case, inverter A11 was kept with original parameters, while only A12 and A13 were modified. Consequently, A12 and A13 are identified as the primary sources of oscillation. The the oscillatory mode has a frequency of 19.2 Hz in the dq reference frame, as shown in Fig. 8. Fig. 9 shows the damping contributions of each device, computed from the model using the Modal Analysis App of SimplusGT. It is evident that inverters A12 and A13 are the main contributors of negative damping, while inverter A11 provides a positive damping contribution.

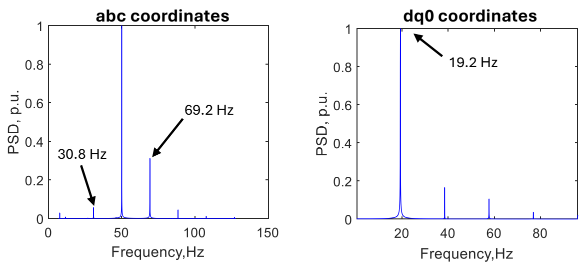

Fig. 8. Power spectral density in Case 4. Line current of A12 in the abc frame and active power of A12 in the $dq0$ frame.

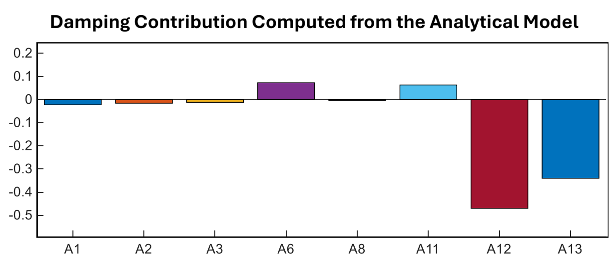

Fig. 9. Damping contribution to the Ω=19.2 Hz mode in Case 4, calculated from analytical model according to the methodology of [6]

III. Grid Following Inverters-based Forced Oscillations

Unlike natural oscillations, which are associated with the intrinsic dynamic modes of the power system, forced oscillations (FOs) are driven by sustained excitations whose frequency is determined by the disturbance source. Typical examples include malfunctioning or poorly tuned plant-level controllers, improper operation of individual inverter control loops, erroneous measurement channels, or auxiliary control functions that unintentionally introduce periodic components into the active or reactive power references of individual inverters [21].

For the FO tests, a slightly modified GFL inverter model was adopted, in which the current references are directly defined as $i_d^* = \frac{P_{\text{ref}}}{V}$ and $i_q^* = \frac{Q_{\text{ref}}}{V}$, where P_{ref} and Q_{ref} denote the active and reactive power references, respectively, and V is the magnitude of the inverter terminal voltage.

Forced oscillations (FOs) were injected into the active and reactive power references P_{ref} and Q_{ref} of the IBRs, one at a time, resulting in six test cases. The base case was generated from Case 3, with the current-control bandwidth of A12 f_i increased from 320 Hz to 350 Hz, ensuring that all natural modes have a damping factor greater than 10%. The FO frequency in all cases was set to 7 Hz, with an amplitude of 0.05 pu. Leveraging the open-source nature of SimplusGT, the FO was implemented by modifying the inverter model source code, adding a sinusoidal signal with the desired frequency and amplitude to the corresponding control reference.

IV. Grid Forming Inverters-based Natural Oscillations

Two GFM inverters were added at buses 4 and 5, as shown in Fig. 10, denoted as A4 and A5. In this case, the GFM inverters were placed at relatively stronger buses than the GFL inverters, while being located at adjacent nodes in order to promote an oscillation mechanism between them.

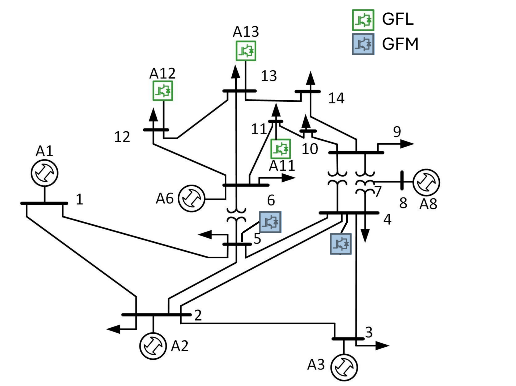

Fig. 10. Modified IEEE 14-bus system with GFL inverters connected at buses 11, 12, 13, and GFM inverters at buses 4 and 5, [16].

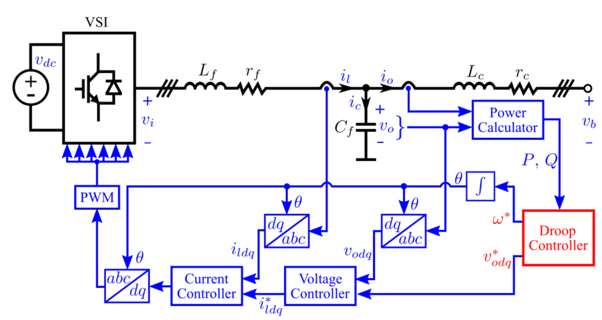

Fig. 11. Droop-controlled GFM Inverter [22]

The control scheme of the GFM inverter is illustrated in Fig. 11. The GFM inverter adopts a hierarchical control structure composed of outer power–frequency and voltage–reactive power droop loops, a voltage control loop, and inner current control loops. The droop controller generates the frequency reference ω^* and the voltage reference v_{odq}^* based on the measured active and reactive powers. The frequency reference is integrated to obtain the voltage angle used for the dq transformations, enabling self-synchronization through power-angle dynamics, without relying on a PLL. In contrast to GFL inverters, which require a PLL to track the grid voltage angle and inject currents synchronized to an externally imposed voltage, the GFM inverter establishes its own voltage waveform and

979-8-3315-8138-1

inherently synchronizes with the network through its droop characteristics. The voltage controller regulates the converter terminal voltage to track v^*_{odq} and produces the reference currents i^*_{dq}, which are enforced by inner current control loops. The controller outputs are then translated into modulation signals through the PWM stage to drive the inverter switches.

The GFM inverter model is characterized by the following parameters: filtering inductor inductance and resistance (L_f, R_f), filtering capacitor (C_f), coupling inductor inductance and resistance (L_c, R_c), frequency droop gain (D_w) and bandwidth (f_droop), voltage droop gain (D_v), voltage control bandwidth (f_vdq), and current control bandwidth (f_idq).

The characteristics of the droop controllers are: $\omega^* = [W_{r0} + D_w (P_0 - P)] \times \mathrm{LPF}$, $v^*_{od} = v_{od0} + D_v (Q_0 - Q)$ and $v^*_{oq} = 0$. P_0 and Q_0 are the active and reactive power setpoints, respectively, W_{r0} and v_{od0} are the setpoints of the angular frequency and the d-axis voltage, respectively. LPF denotes a low-pass filter whose bandwidth is defined by f_droop.

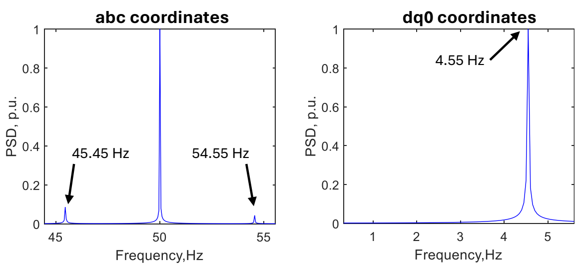

Fig. 12. Power spectral density in GFM Case. Line current of A5 in the abc frame and active power of A12 in the $dq0$ frame.

A control interaction between these GFM inverters was induced by reducing the voltage control bandwidth of A5 until sustained oscillations at 4.55 Hz were observed (Fig. 12). The parameters for both GFM inverters are as follows: $\omega L_\mathrm{f} = 0.05$, $R_\mathrm{f} = 0.01$, $\omega C_\mathrm{f} = 0.015$, $\omega L_\mathrm{c} = 0.01$, $R_\mathrm{c} = 0$, $D_\omega = 0.01$, $f_\mathrm{droop} = 1$ Hz, $D_v = 0$, and $f_\mathrm{idq} = 600$ Hz. The voltage control bandwidth differs between the two GFMs: $f_\mathrm{vdq} = 420$ Hz for inverter A4, and $f_\mathrm{vdq} = 360$ Hz for A5.

V. Conclusions

The simulated scenarios cover a range of parameter configurations leading to subsynchronous oscillations, including both natural and forced oscillations involving grid-following and grid-forming inverters. The generated point-on-wave dataset offers a valuable benchmark for evaluating and comparing subsynchronous oscillations localization methods, supporting future research and development in power system stability analysis. The dataset is publicly available through the IEEE Task Force on Forced Oscillations dataset library [14].

References

[1] CIGRE, "Guidelines for subsynchronous oscillation studies in power electronics dominated power systems," *Technical Brochure 909*, June 2023.

[2] Y. Cheng, L. Fan, J. Rose, S.-H. Huang, J. Schmall, X. Wang, X. Xie, J. Shair, J. R. Ramamurthy, N. Modi, C. Li, C. Wang, S. Shah, B. Pal, Z. Miao, A. Isaacs, J. Mahseredjian, and J. Zhou, "Real-world subsynchronous oscillation events in power grids with high penetrations of inverter-based resources," *IEEE Transactions on Power Systems*, vol. 38, no. 1, pp. 316–330, 2023.

[3] W. Xu, J. Yong, H. J. Marquez, and C. Li, "Interharmonic power – a new concept for power system oscillation source location," *IEEE Transactions on Power Systems*, pp. 1–13, 2025.

[4] R. K. Varma and A. Moharana, "SSR in double-cage induction generator-based wind farm connected to series-compensated transmission line," *IEEE Transactions on Power Systems*, vol. 28, no. 3, pp. 2573–2583, 2013.

[5] J. Sun, "Impedance-based stability criterion for grid-connected inverters," *IEEE Transactions on Power Electronics*, vol. 26, no. 11, pp. 3075–3078, 2011.

[6] Y. Zhu, Y. Gu, Y. Li, and T. C. Green, "Participation analysis in impedance models: The grey-box approach for power system stability," *IEEE Transactions on Power Systems*, vol. 37, no. 1, pp. 343–353, 2022.

[7] Z. Lei, L. Chen, F. Chang, L. Li, M. Zhang, and Y. Min, "Analysis and comparison of sub/super-synchronous oscillation source location methods," in *2023 IEEE 7th Conference on Energy Internet and Energy System Integration (EI2)*, 2023, pp. 2581–2587.

[8] L. Chen, Y. Min, and W. Hu, "An energy-based method for location of power system oscillation source," *IEEE Trans. on Power Syst.*, vol. 28, no. 2, pp. 828–836, 2013.

[9] S. Maslennikov, B. Wang, and E. Litvinov, "Dissipating energy flow method for locating the source of sustained oscillations," *Int. J. Elec. Power*, vol. 88, pp. 55 – 62, 2017.

[10] P. G. Estevez, P. Marchi, C. Galarza, and M. Elizondo, "Complex dissipating energy flow method for forced oscillation source location," *IEEE Transactions on Power Systems*, vol. 37, no. 5, pp. 4141–4144, 2022.

[11] Y. Chen, Z. Fan, D. Gregory, X. Zhou, and R. Rabbani, "A survey of oscillation localization techniques in power systems," *IEEE Access*, vol. 13, pp. 28 836–28 860, 2025.

[12] B. Wang, S. Maslennikov, and K. Sun, "Descriptor: Phasor measurement unit dataset for oscillation source location (pmu-osl)," *IEEE Data Descriptions*, pp. 1–8, 2025.

[13] Yitong Li. (2024) Simplus Grid Tool. [Online]. Available: https://github.com/Future-Power-Networks/Simplus-Grid-Tool

[14] Kai Sun, Slava Maslennikov, Bin Wang. (2025) Test Cases Library on Forced/Sustained Power System Oscillations. [Online]. Available: https://ieee-dataport.org/documents/test-cases-library-forcedsustained-power-system-oscillations

[15] Kai Sun, Jim Follum, Bin Wang. (2025) IEEE PES Task Force on Forced Oscillations. [Online]. Available: https://web.eecs.utk.edu/~kaisun/FOTF/

[16] Y. Zhu, H. Karbouj, X. Zhou, and Y. Gu, "Unified dissipation energy flow," Aug. 2024. [Online]. Available: http://dx.doi.org/10.36227/techrxiv.172348945.56366598/v1

[17] University of Cyprus. (2025) IEEE 14-bus modified test system. [Online]. Available: https://www2.kios.ucy.ac.cy/testsystems/index.php/ieee-14-bus-modified-test-system/

[18] Yue Zhu. (2024) Cases 1-3 Simplus Data. [Online]. Available: https://github.com/Future-Power-Networks/Simplus-Grid-Tool/tree/2023July_DEF

[19] Y. Li, Y. Gu, and T. C. Green, "Revisiting grid-forming and grid-following inverters: A duality theory," *IEEE Transactions on Power Systems*, vol. 37, no. 6, pp. 4541–4554, 2022.

[20] Y. Zhu, Y. Gu, Y. Li, and T. C. Green, "Impedance-based root-cause analysis: Comparative study of impedance models and calculation of eigenvalue sensitivity," *IEEE Transactions on Power Systems*, vol. 38, no. 2, pp. 1642–1654, 2023.

[21] T. Surinkaew, K. Emami, R. Shah, S. Islam, and N. Mithulananthan, "Forced oscillation in power systems with converter controlled-based resources–a survey with case studies," *IEEE Access*, vol. 9, pp. 150 911–150 924, 2021.

[22] Y. Li, Y. Gu, Y. Zhu, A. Junyent-Ferré, X. Xiang, and T. C. Green, "Impedance circuit model of grid-forming inverter: Visualizing control algorithms as circuit elements," *IEEE Transactions on Power Electronics*, vol. 36, no. 3, pp. 3377–3395, 2021.